Epitaxial and Strong Support Interactions between Pt and $LaFeO_3$ Films Stabilize Pt Dispersion

Xinyu Mao, Alexandre C. Foucher, Tiziano Montini, Eric A. Stach, Paolo Fornasiero, and Raymond J. Gorte*

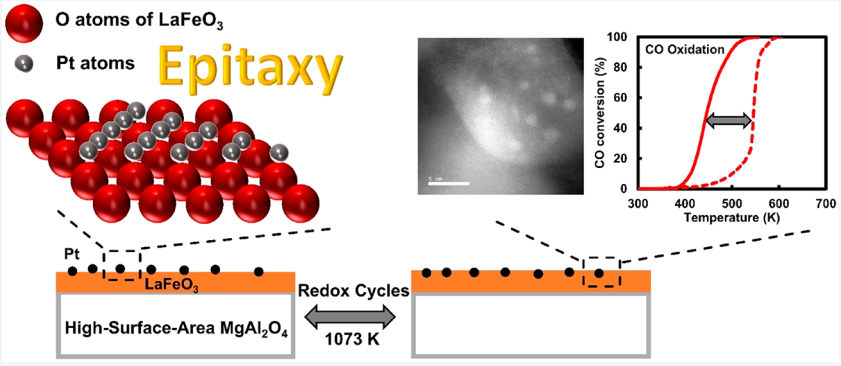

ABSTRACT: The ability to stabilize very small Pt crystallites in supported-metal catalysts following harsh treatments is an important industrial problem. Here, we demonstrate that Pt particles can be maintained in the 1- to 2-nm range following multiple oxidation and reduction cycles at 1073 K when the particles are supported on 0.5-nm $LaFeO_3$ films that have been deposited onto $MgAl_2O_4$ using atomic layer deposition. Characterization by scanning transmission electron microscopy suggests that when the catalyst is oxidized at 1073 K, the Pt crystallites are oriented with respect to the underlying $LaFeO_3$. X-ray absorption spectroscopy also shows evidence of changes in the Pt environment. CO-oxidation rates for the reduced catalyst remain unchanged after five redox cycles at 1073 K. Epitaxial growth of Pt clusters and the consequent strong metal−support interaction between Pt and $LaFeO_3$ are suggested to be the main reasons for the enhanced catalytic performances.

1. INTRODUCTION

Deactivation of supported-metal catalysts due to sintering of the metal particles is an important problem for high-temperature catalysis applications, such as automotive emissions control. One proposed solution to this problem involves the use of mixed-oxide supports with the perovskite structure because, in specific cases, catalytic metal atoms can reversibly enter and leave the oxide lattice after high-temperature oxidation or reduction treatments.[1−3] Reversible "ingress" of large metal particles and "egress" of small particles could therefore allow redispersion of deactivated catalysts. However, the concept has not been entirely successful. After high-temperature treatments, the perovskites that are capable of exsolving catalytic metals are usually composed of large crystallites with low surface areas. In at least some cases, a significant fraction of the metal particles that exsolve from the perovskite lattice remain embedded in the bulk of the perovskite crystallites, making them unavailable for catalyzing reactions.[4,5] Large crystallites likely also contribute to the fact that the kinetics of metal ingress are too slow to be practical.[6,7]

To avoid the issues associated with bulk perovskites, we have prepared the perovskite, $LaFeO_3$, as a thin film on high-surface-area $MgAl_2O_4$ by atomic layer deposition (ALD) and used this as the support for precious metals.[8] A 0.5-nm uniform film of $LaFeO_3$ (density of 6.65 g/cm^3) on a 120 m^2/g substrate results in a material that is 28.5 wt % perovskite. Thus, we hypothesize that even relatively high loadings of the perovskite lead to films that are so thin that the egress−ingress of large metal particles is not likely to occur. However, the present work will show that strong chemical interactions between Pt and the $LaFeO_3$ films are able to dramatically stabilize small metal particles, even after multiple high-temperature, oxidation−reduction cycles. The chemical bonding in the oxidized samples is observed directly through the formation of Pt

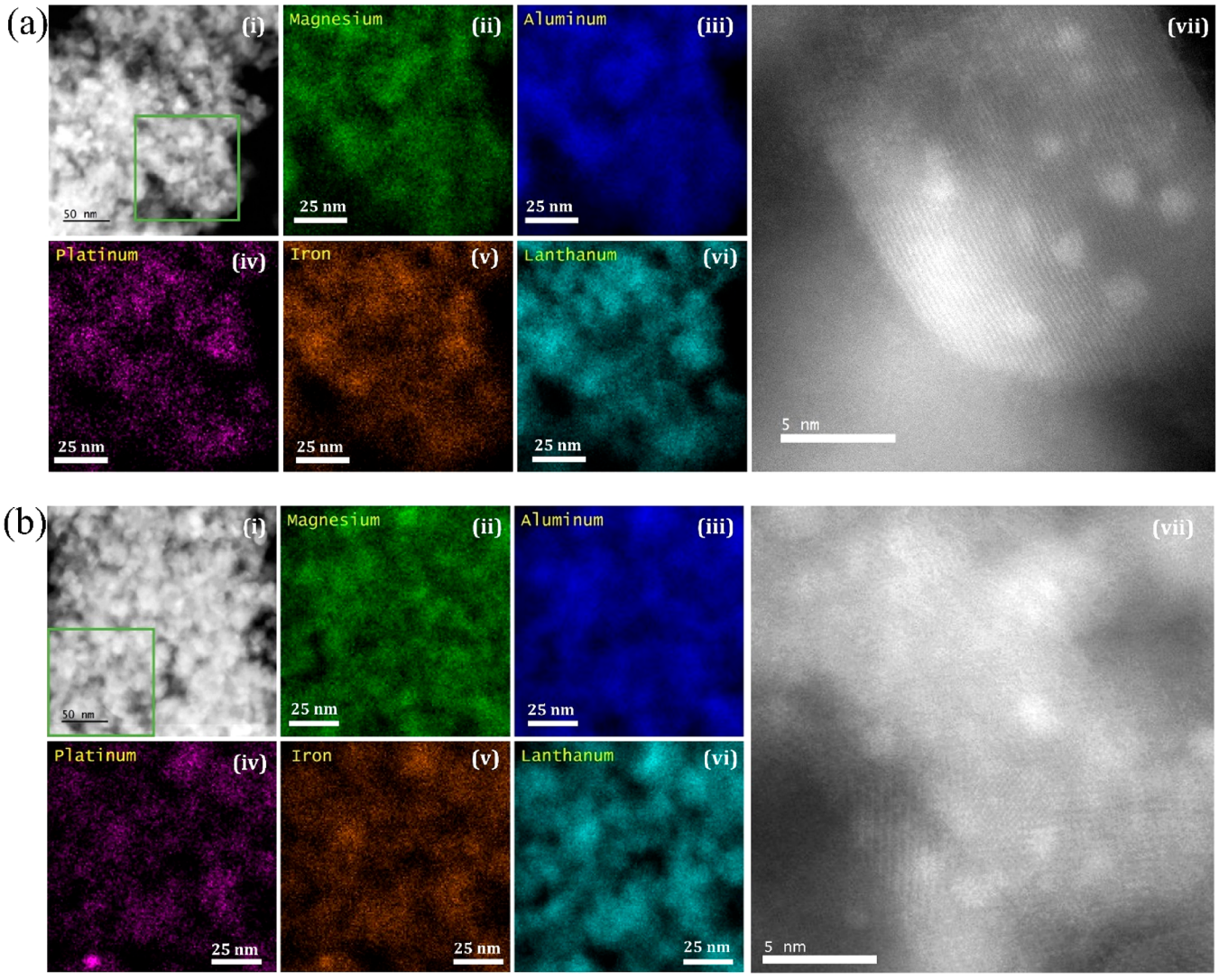

Figure 1. (a) High-angle annular dark-field STEM image (i) and EDS maps (ii–vi) of Mg, Al, Pt, Fe, and La on the oxidized Pt/$LaFeO_3$/$MgAl_2O_4$ after 5 redox cycles, taken from the region indicated by the green box. High-angle annular dark-field STEM image with larger magnification (vii) on the same sample. (b) High-angle annular dark-field STEM image (i) and EDS maps (ii–vi) of Mg, Al, Pt, Fe, and La on the reduced Pt/$LaFeO_3$/$MgAl_2O_4$ after 5 redox cycles, taken from the region indicated by the green box. High-angle annular dark-field STEM image with larger magnification (vii) on the same sample.

particles that are epitaxially aligned with respect to $LaFeO_3$ crystallites. The results suggest that perovskite-supported metals may provide a solution to the sintering problem in some applications.

2. EXPERIMENTAL METHODS

$MgAl_2O_4$ was prepared in our laboratory by coprecipitation of Mg and Al nitrate salts, using $(NH_4)HCO_3$ solutions. After calcination to 1173 K, the powders were washed in concentrated HNO_3 and rinsed in distilled water to remove all but the $MgAl_2O_4$ phase. After this treatment, the $MgAl_2O_4$ powder had a BET surface area of 120 m^2/g and X-ray diffraction (XRD) confirmed that only the $MgAl_2O_4$ phase existed. The $LaFeO_3$ films were deposited onto the $MgAl_2O_4$ support by ALD, using procedures described elsewhere.[8] The ALD precursors were $La(TMHD)_3$ (TMHD = 2,2,6,6-tetramethyl-3,5-heptanedionato, Strem Chemicals, Inc.), and ferrocene ($Fe(Cp)_2$, Sigma-Aldrich). For each ALD cycle, the substrate was exposed to the ferrocene or $La(TMHD)_3$ vapors multiple times at 523 K to ensure surface saturation of the precursor. The ferrocene was oxidized by exposing the sample to 1 atm of O_2 in the ALD system at 523 K for 300 s; however, the $La(TMHD)_3$ could not be fully oxidized by these conditions. To oxidize the adsorbed $La(TMHD)_3$, we placed the sample in a muffle furnace at 873 K for 60 s. The growth rates for the individual oxides were shown, gravimetrically, to be linear, with values of 3.4×10^{17} La atoms/cycle·m^2 (0.014-nm La_2O_3/cycle) and 1.0×10^{18} Fe atoms/cycle·m^2 (0.025-nm Fe_2O_3/cycle). Films with the correct perovskite stoichiometry were obtained by alternating between 3 ALD cycles of La_2O_3 and 1 ALD cycle of Fe_2O_3. The final loading of $LaFeO_3$ in this study, 30 ± 1.5 wt %, was confirmed by inductively coupled plasma-optical emission spectrometry (ICP-OES). The BET surface area of $LaFeO_3$/$MgAl_2O_4$ after calcination at 873 K was 78 m^2/g.

To ensure that there was good initial contact between the Pt and the $LaFeO_3$ support, we added Pt by ALD using 1 cycle of platinum(II) acetylacetonate (Strem Chemicals, Inc.). The Pt was deposited onto the support prior to the final calcination step (i.e., the $LaFeO_3$/$MgAl_2O_4$ sample had been calcined to only 873 K prior to addition of Pt). After the addition of Pt, the catalyst was oxidized with air in a muffle furnace at 573 K to remove the ligands. The Pt loading for the samples was measured by ICP-OES to be 2.9 ± 0.2 wt % (~1.1×10^{18} Pt/m^2), which is comparable to the previously reported growth rate of Pt for this precursor.[9] Because our interest in the Pt-$LaFeO_3$/$MgAl_2O_4$ catalysts was in understanding the stability of these

catalysts following high-temperature oxidation and reduction, samples were exposed to 5 oxidation and reduction cycles at 1073 K prior to the characterization shown in this paper. The oxidation cycles were carried out in 10% O_2—He for 1 h and the reduction cycles flowing 10% H_2—He mixtures for 1 h, and the total flow rate was maintained at 100 mL/min.

The ALD-prepared samples were characterized initially by XRD using a Rigaku Smartlab diffractometer equipped with a Cu Kα source (λ = 0.15416 nm), but additional measurements were subsequently performed on a Philips X'Pert diffractometer equipped with a Cu Kα source in the range 10°—100° with a step of 0.02°. Rietveld analysis was performed using the PowderCell 2.4 program. Crystallite sizes were calculated by applying Scherrer's equation to the main reflections of each crystalline phase in the region from 25° to 40°. For CO chemisorption measurements, samples were reduced in 200 Torr H_2 at 473 K before CO uptakes were measured at room temperature. ICP-OES was performed on a Spectro Genesis spectrometer with a Mod Lichte nebulizer. Initial scanning transmission electron microscopy (STEM) and energy dispersive X-ray spectra (EDS) measurements were performed with a JEOL JEM-F200 STEM, operated at 200 kV; STEM images with high magnification were taken using a JEOL NEOARM STEM. Powder specimens were diluted in isopropanol and put on lacey carbon films on copper grids (Electron Microscopy Sciences).

Ex situ XANES/EXAFS spectra were acquired on the SAMBA beamline at synchrotron SOLEIL (Gif-sur-Yvette, France) at the Pt L_3 edge (11563.7 eV).[10] Spectra were collected by measuring the Kα fluorescence line with a 36 pixels germanium detector (Canberra), whereas transmission data were simultaneously recorded with ionization chambers (IC-SPEC, FMB-Oxford) for the sample and Pt foil as the standard. Data analysis was performed with the DEMETER software suite.[11]

Simultaneous temperature-programmed desorption/thermogravimetric analysis (TPD/TGA) measurements were performed using equipment that is described in detail elsewhere.[12] In these measurements, the sample was saturated with the vapor from liquid 2-propanol at room temperature and then evacuated for 1 h to a base pressure of 10^{-8} Torr. The TPD/TGA measurements were performed by ramping the sample temperature at 10 K/min while monitoring the partial pressures with a residual-gas analyzer.

Differential, steady-state rates were measured over 0.1-g samples in a $^1/_4$-in. quartz tubular flow reactor. Products were detected with an online gas chromatograph (SRI8610C) equipped with a Hayesep Q column and a TCD detector. Most CO-oxidation rates were measured with the total gas flow rate maintained at 100 mL/min using a He carrier and partial pressures of CO and O_2 maintained at 25 and 12.5 Torr, respectively. To study the dependence of CO-oxidation rates on the partial pressure of CO, we kept the total flow rate and flow rate of O_2 constant at 100 and 1 mL/min, but P_{CO} was varied by changing the flow rates of He and CO. Before the measurements were taken, the Pt catalysts were either oxidized or reduced in a 10% gas mixture of either O_2 or H_2 in He at a total flow rate of 100 mL/min. Light-off reaction measurements for CO oxidation were also measured over 0.1-g samples in a tubular flow reactor in which the products could be continuously monitored using a residual-gas analyzer (SRS-RGA-100). The flow rates of He, CO, and O_2 were the same as those used for differential, steady-state rates. The temperature ramp rate was 10 K/min.

3. RESULTS

3.1. TPD/STEM/XRD. Assuming the $LaFeO_3$ uniformly covered the 120 m^2/g $MgAl_2O_4$ support, a simple mass balance indicates that a loading of 30 wt % corresponds to a film 0.56-nm-thick if the $LaFeO_3$ has its bulk density of 6.65 g/cm^3. Evidence for film uniformity came from multiple sources. First, HAADF-STEM/EDS measurements were performed to determine the morphology of the Pt/$LaFeO_3$/$MgAl_2O_4$ samples. Figure 1a,b provide images, together with the EDS maps, for an oxidized and reduced sample after the sample had already undergone five oxidation and reduction cycles at 1073 K. In both cases, the lower resolution HAADF-STEM images in the upper left-hand panels are indistinguishable from those of the $MgAl_2O_4$ support. More informative are the EDS maps, which show that La, Fe, and Pt each uniformly cover the surface after either oxidation or reduction. The EDS intensity variations for all three elements also overlap reasonably well with intensity variations for Mg and Al from the support. STEM/EDS scans for the oxidized sample with lower magnification are shown in Figure S1 (Supporting Information) and further confirm that La and Fe uniformly cover the support surface.

Additional evidence for film uniformity came from TPD/TGA measurements of adsorbed 2-propanol, performed on the unmodified $MgAl_2O_4$ and the oxidized Pt/$LaFeO_3$/$MgAl_2O_4$ that had been treated with 5 redox cycles. These data are shown in Figure S2. $MgAl_2O_4$ exhibits Lewis-acid characteristics and most of the 2-propanol that is adsorbed at room temperature undergoes dehydration to propene and water in a sharp reaction feature at 450 K in TPD. The $MgAl_2O_4$ feature is completely absent in the TPD/TGA results for Pt/$LaFeO_3$/$MgAl_2O_4$. Most of the adsorbed 2-propanol also reacted during TPD on this sample, but all of the reaction occurred at temperatures higher than 450 K. Furthermore, a large fraction of the product formed from 2-propanol was acetone. If any of the $MgAl_2O_4$ had been exposed, a feature at 450 K should have been observed. Given that the average film thickness was only 0.56 nm, it is unlikely that there could be larger perovskite crystallites with sufficient $LaFeO_3$ remaining to cover the surface of the $MgAl_2O_4$.

Although the uniform coverage of $LaFeO_3$ over the $MgAl_2O_4$ surface had been established previously for ALD preparation,[8] the fact that these films are stable to multiple redox cycles at 1073 K is encouraging. It is also encouraging to observe well-dispersed Pt following either oxidation or reduction at 1073 K. The higher-resolution images in the right-hand panels of Figure 1a,b indicate that Pt particles are present on both the oxidized and the reduced samples, but they are irregular in shape and only 1 to 2 nm in size. That the STEM images are representative of the entire sample was demonstrated by the fact that the Pt content calculated from the EDS signals varied from 2.7 to 3.1 wt % on different regions with dispersed Pt, in good agreement with the ICP measurement.

To demonstrate that stabilization of the Pt particles on the Pt/$LaFeO_3$/$MgAl_2O_4$ sample was due to the presence of $LaFeO_3$, we also performed HAADF-STEM measurements on a reduced 3.1 wt % Pt/$MgAl_2O_4$ sample that had undergone 5 redox cycles. The Pt on this sample was again prepared by ALD and had an initial dispersion of 27%. As shown in Figure S3, the redox treatments caused a dramatic growth of the Pt on this sample, with crystallite sizes ranging from 20 to 100 nm. Pt/$MgAl_2O_4$ has previously been reported to be relatively resistant to sintering,[13] making the high dispersion of Pt/$LaFeO_3$/$MgAl_2O_4$ sample even more noteworthy.

A closer inspection of the high-resolution STEM image of the oxidized sample, shown in Figure 2, suggests that the small Pt particles on the oxidized sample are aligned with the underlying $LaFeO_3$ lattice. That these are indeed Pt crystallites was confirmed by the EDS mapping with the signals of Pt M and Pt L emitted X-rays shown in Figure S4. The images show distinct registry of the Pt atoms on top of the rows of $LaFeO_3$.

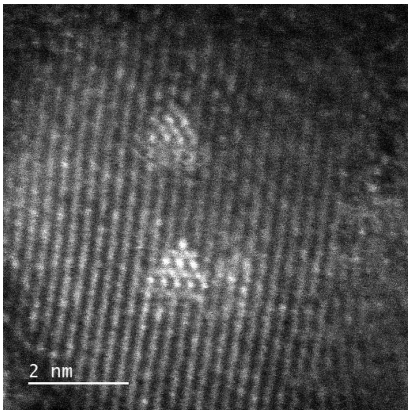

Figure 2. High-angle annular dark-field STEM image of the oxidized $Pt/LaFeO_3/MgAl_2O_4$ after 5 redox cycles at 1073 K.

Other images of this sample, reported in Figure S5, also show very small Pt clusters that are oriented along the same direction with the $LaFeO_3$ lattice. Higher-resolution STEM images of the reduced sample are shown in Figure 3 and Figure

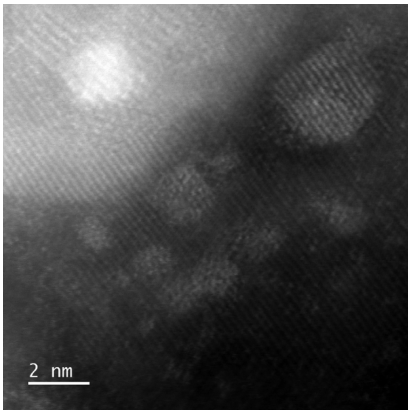

Figure 3. High-angle annular dark-field STEM image of the reduced $Pt/LaFeO_3/MgAl_2O_4$ after 5 redox cycles at 1073 K.

S6. The range of particle sizes is similar but slightly larger than that with the oxidized samples. What is different is that at least some of the Pt crystallites are not oriented with respect to the underlying perovskite lattice.

XRD measurements were performed to determine the structure of the deposited films, with results reported in Figure 4. The bottom pattern, Figure 4i, is that of the $MgAl_2O_4$ support, whereas the patterns for the oxidized (Figure 4ii and reduced (Figure 4iii samples with 2.9 wt % Pt and 30 wt % $LaFeO_3$ are shown above it. The XRD patterns in this figure were obtained on the same sample whose STEM images are shown in Figure 1. First, both the oxidized and reduced samples show intense peaks for the perovskite phase, without major changes due to pretreatment, indicating that the perovskite phase is reasonably stable. On the basis of the line widths (see Table 1), the crystallite size of the perovskite phase is on the order of 10 nm, which appears to contradict the earlier conclusion that the $LaFeO_3$ exists in the form of a 0.56-nm $LaFeO_3$ film. It is possible that a small part of $LaFeO_3$ films agglomerated into large crystallites that were not observed in STEM, leaving sufficient $LaFeO_3$ to cover the rest of the surface, but this would not explain the high intensity of the perovskite features. Two-dimensional crystallites could exhibit

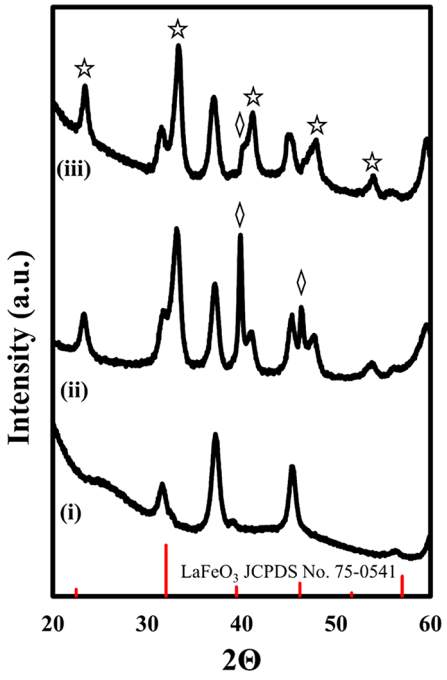

Figure 4. XRD patterns of (i) unmodified $MgAl_2O_4$, (ii) oxidized $Pt/LaFeO_3/MgAl_2O_4$ after 5 redox cycles at 1073 K, and (iii) reduced $Pt/LaFeO_3/MgAl_2O_4$ after 5 redox cycles at 1073 K. Perovskite features are marked with stars and metallic Pt with diamonds.

intense diffraction peaks but only in the directions perpendicular to the larger length scale.[14] Therefore, a $LaFeO_3$ film in the form of two-dimensional crystallites, oriented in random directions, possibly with respect to the underlying $MgAl_2O_4$ grains, would be expected to exhibit a standard XRD powder pattern.

The major difference in the patterns for the oxidized and reduced samples is in the presence of very intense Pt features for the oxidized sample, which decrease dramatically in height after reduction. This result is surprising for multiple reasons. First, the intense, narrow Pt feature appears to be inconsistent with the observation of well-dispersed Pt in the STEM images. Second, high-temperature reduction would normally increase metal particle size, not decrease particle size, and this should cause the Pt peaks to sharpen and increase in height. Finally, it is important to recognize that this sample had been oxidized and reduced five times at 1073 K prior to acquiring the diffraction patterns, and the transition between the patterns for the oxidized and reduced samples was completely reversible upon calcination or reduction at 1073 K. (XRD patterns for the $Pt/LaFeO_3/MgAl_2O_4$ after the first redox cycle are reported in Figure S7 and do not show any significant difference from those shown in Figure 4.) Particle growth of Pt is usually irreversible.

To better understand the diffraction patterns, we performed Rietveld analysis on a separate sample batch prepared in the same manner. The diffraction patterns used in that analysis, shown in Figure S8, are again identical to those shown in Figure 4. Conclusions from the analysis are summarized in Table 1. First, the Rietveld analysis indicates that the Pt content was approximately 4 wt % for both reduced and oxidized samples and that the change in height and width of the Pt peaks upon reduction is due to an apparent decrease in Pt crystallite size from 22 to 10 nm. Obviously, the estimate of crystallite size does not agree with the STEM results in Figure

Table 1. Results from Rietveld Analysis of the XRD Patterns of the Oxidized and Reduced $Pt/LaFeO_3/MgAl_2O_4$, in Comparison with the Cell Parameters Reported for the Parent Pure Phases

	oxidized			reduced			parent pure phase
phase (space group)	amount (wt %)	cell parameters (nm)	crystallite size (nm)	amount (wt %)	cell parameters (nm)	crystallite size (nm)	cell parameters (nm)
Pt ($Fm\bar{3}m$)	4.4%	a = 0.39172	22	4.1%	a = 0.38980	10	a = 0.39231
$MgAl_2O_4$ ($Fd\bar{3}m$)	64.2%	a = 0.80104	12	66.4%	a = 0.80517	10	a = 0.80806
$LaFeO_3$ ($Pnma$)	16.0%	a = 0.56182, b = 0.76394, c = 0.54441	8.7	6.2%	a = 0.55398, b = 0.77324, c = 0.54456	12	a = 0.56619, b = 0.79447, c = 0.56008
$LaAlO_3$($R\bar{3}c$)	15.4%	a = 0.53967, c = 1.31445	14	21.8%	a = 0.54109, c = 1.31120	13	a = 0.53655, c = 1.31508
La_3FeO_6 ($Cmc2_1$)				1.5%	a = 0.97279, b = 1.21087, c = 0.58461	14	a = 0.94443, b = 1.18767, c = 0.57373

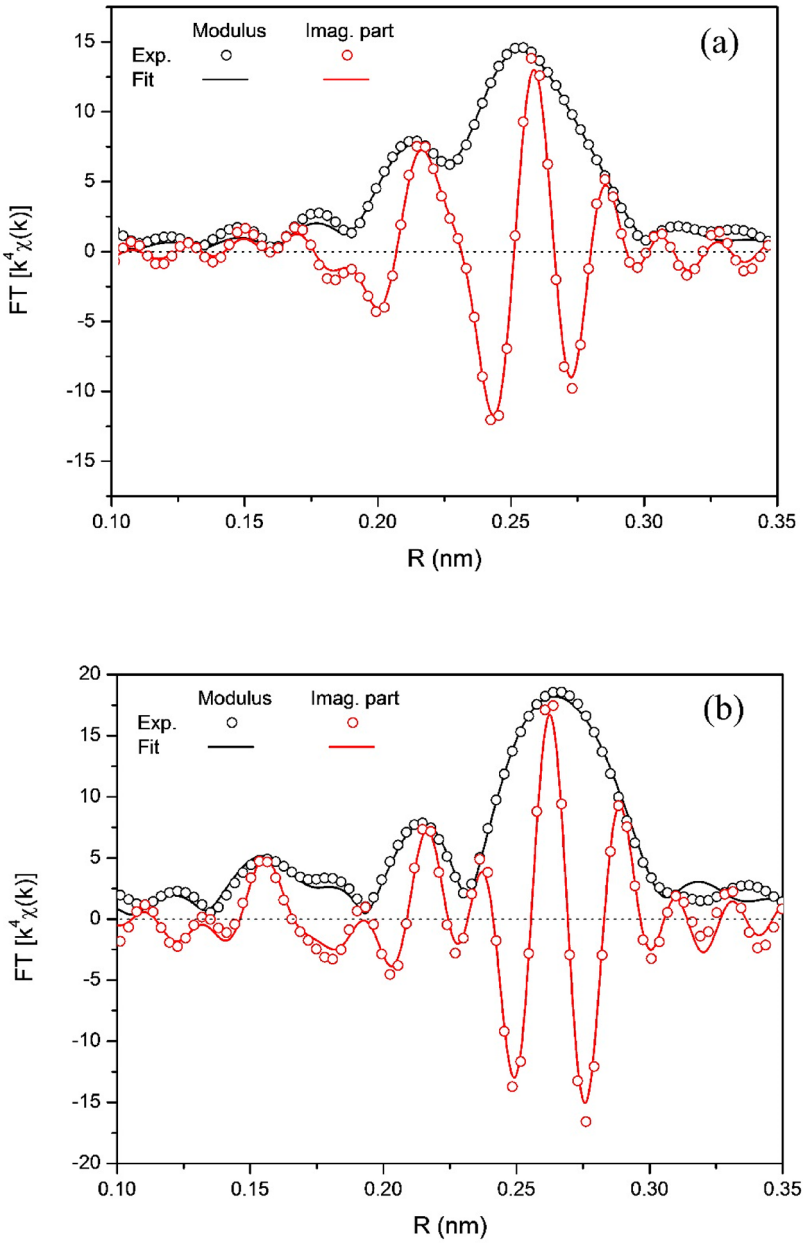

Figure 5. Fit of the experimental k^3-weighted FT-EXAFS signals for the (a) reduced and (b) oxidized $Pt/LaFeO_3/MgAl_2O_4$ samples after 5 redox cycles at 1073 K.

1 but suggests that the redox treatments induce redispersion under reducing conditions and reagglomeration under oxidizing conditions. The estimates of the Pt content on both the oxidized and reduced samples seem in reasonable agreement with the actual Pt content of 2.9 wt % even if, considering the complexity of the sample, the XRD pattern

Table 2. Fitting Results from the Ex Situ EXAFS Analysis at the Pt L_3 Edge for 1073 K Oxidized and Reduced Samples

sample	path	coordination number (CN)	distance R (nm)	$\sigma^2 \times 10^{-5}$ (nm^2)
reduced Pt/$LaFeO_3$/$MgAl_2O_4$	Pt–Fe	3.3 ± 0.9	0.267 ± 0.001	6 ± 2
	Pt–Pt	4.7 ± 0.6	0.273 ± 0.001	4 ± 2
oxidized Pt/$LaFeO_3$/$MgAl_2O_4$	Pt–O	1.8 ± 0.4	0.198 ± 0.001	2 ± 2
	Pt–Pt	8.3 ± 0.7	0.276 ± 0.001	5 ± 2

cannot exclude the presence of a significant number of smaller Pt particles. On the basis of the size of the calculated unit cell for Pt, 0.38980 nm compared to 0.39231 nm for pure Pt, the amount of reduced Fe alloyed with Pt, if present, is very limited. There is no evidence for the formation of crystalline PtO_2 or of metallic Fe. The Rietveld analysis also suggests there may be an evolution of oxide phases during redox cycling. In particular, the analysis indicates that contact between the $LaFeO_3$ and $MgAl_2O_4$ may allow reversible solid-state reaction between these two phases. The cell parameters determined for each oxide phase significantly differ from the theoretical values of the parent phases, suggesting the presence of doping ions in significant amounts. On the basis of the ionic radii of the various cations (Mg^{2+}, Al^{3+}, La^{3+}, and Fe^{3+}),[15] the trends observed in the cell parameters are compatible with the mutual exchange between Mg^{2+} and La^{3+} and between Al^{3+} and Fe^{3+}. Notably, the relative amounts of the different phases differ depending on the thermochemical treatment applied to the materials and a new phase (La_3FeO_6) appears in the reduced sample. For all the oxide phases, the mean crystallite sizes are between 8 and 12 nm (Table 1). It should be noted that any MgO or FeO_x phases that must form if reaction occurs could not be distinguished, possibly because they are amorphous. Finally, considering the complexity of the XRD patterns and the high number of phases identified, a reliable determination of the exact composition of the different oxide phases is not possible.

For comparison, XRD patterns and Rietveld analysis were also performed on the Pt/$MgAl_2O_4$ sample after 5 redox cycles, with results shown in Table S1 and Figure S9. The analysis indicates that the Pt particles supported on $MgAl_2O_4$ have an average size of ~20 nm, in good agreement with the STEM images. Unlike the case for Pt/$LaFeO_3$/$MgAl_2O_4$, no reversible changes in particle size or composition were observed upon redox cycling over samples of Pt/$MgAl_2O_4$.

3.2. XANES/EXAFS. To gain further insight into the nature of the interactions of Pt nanoparticles with $LaFeO_3$, we acquired XAS spectra with a focus on Pt. The XANES spectrum at the Pt L_3 edge of the reduced Pt/$LaFeO_3$/$MgAl_2O_4$ sample (Figure S10a) is similar to that of Pt foil, indicating that all of the Pt atoms are in the zerovalent state. Differences between the reduced sample and the Pt foil can be observed in the EXAFS part of the spectrum. The extracted EXAFS signal (Figure S11a) resembles that obtained from Pt foil but shows a lower intensity and a lower frequency. Attempts to model the EXAFS signal with a single Pt–Pt distance did not provide a reasonable fit of the experimental data. This was achieved only by introducing a Pt–Fe path at a distance slightly shorter than the Pt–Pt distance. The obtained fit (R-factor = 0.0060) is presented in Figure 5a, whereas the contributions of each path to the FT-EXAFS signal are presented in Figure S11b. The structural parameters extracted from this fitting are shown in Table 2. It is worth noting the absence of a relevant feature associated with a Pt–O distance near R = 0.20 nm (R_{eff} = 0.16 nm), as might be expected for Pt atoms on the surface of metal nanoparticles and interaction with the support. This fact may suggest the formation of a thin layer of reduced Fe atoms at the interface between the support and the small Pt nanoparticles. This is also consistent with there being an important contribution from the Pt–Fe path (at a distance slightly shorter than Pt–Pt in Pt metal (see Table 2 and Figure S11) and the lack of a direct interaction of Pt nanoparticles with the oxide support.

The XANES/EXAFS results for the oxidized Pt/$LaFeO_3$/$MgAl_2O_4$ were significantly different. The white-line intensity in the XANES spectrum (Figure S10b) was intermediate between that observed for Pt metal and PtO_2. Linear combination analysis indicated that 69% of Pt is in the zerovalent state, whereas 31% was present as oxidized Pt ions. The EXAFS signal at the Pt L_3 edge in the oxidized Pt/$LaFeO_3$/$MgAl_2O_4$ sample (Figure S12a) significantly differs from that of the reduced sample, becoming more similar to (and being dominated by) a contribution from metallic Pt. Two contributions related to Pt–O and metal Pt–Pt paths can be clearly observed in the FT-EXAFS signal (Figure S12b). Modeling of the EXAFS signal included these two paths, with the result presented in Figure 5b) (R-factor = 0.0070) and the structural parameters reported in Table 2. The combination of XANES and EXAFS results on oxidized Pt/$LaFeO_3$/$MgAl_2O_4$ indicates that the Pt exists primarily in the reduced state, even if some reoxidation occurs by passivation of the surface and/or at the interface with the support. It is noteworthy that the Pt–Fe path is lost after reoxidation of the sample, consistent with changes in the Fe-containing phases observed by XRD analysis.

One possible way to understand the EXAFS results is that a layer of oxygen atoms between Pt and the $LaFeO_3$ support is removed upon reduction so that Pt contacts Fe in the reduced sample. The oxygen atoms are then inserted back after oxidation, leading to a strong bond between Pt and $LaFeO_3$. This bonding could be responsible for the epitaxial registration and for maintaining high Pt dispersion. It is noteworthy that the calculated coordination number for Pt in the oxidized sample was 8.3, suggesting a Pt particle size in the same range observed in STEM, 1–2 nm assuming a cuboctahedral morphology.[16]

There is an obvious discrepancy between the Pt particle sizes obtained from XRD, from STEM, and from XAS. This can be rationalized only by considering differences in what the techniques measure. XRD is sensitive only to that fraction of the sample that has a high degree of crystallinity, and small particles would not contribute to the pattern. If there is a distribution of Pt particle sizes, XRD could therefore overestimate the actual mean crystallite size. Furthermore, preferential orientation of particles could modify the intensity and width of the various reflections.[14] EXAFS, on the other hand, is particularly sensitive to smaller nanoparticles and the coordination number can change dramatically for even minor changes in size.[16] This can result in the crystallite size being underestimated. Although the STEM measurements in this study showed only very small particles, it must be acknowl-

edged that the images sample only a fraction of the sample and may not be representative of the overall composition.

Several different scenarios can be used to explain the results. The first is that the Pt particles exist in a bimodal distribution. In this picture, the Pt XRD peaks for the oxidized sample are due mainly to the fraction of larger Pt particles, whereas the STEM and EXAFS over-represent smaller particles. This model is compatible with the epitaxial registration observed for the small Pt nanoparticles but would require reversible sintering of the Pt upon oxidation and spreading of Pt particles upon reduction. The Pt coordination number of 8.3 observed for the oxidized sample would be an average of that for small and large particles. Indeed, if only 69% of oxidized catalyst has Pt in the metallic form, the actual CN of Pt in the metal nanoparticles is close to 12, the value for bulk Pt. The scenario would require 69% of the Pt to be present in the form of large metal particles and 31% in the form of isolated Pt atoms, neither of which was observed in HAADF-STEM. A second possible model is that the intense Pt diffraction feature observed in XRD on the oxidized sample is due to scattering from collections of small Pt clusters, oriented with respect to each other, on much larger, two-dimensional perovskite crystallites. After reduction, the epitaxy is partially lost, accounting for the increased width and decreased height of the Pt peaks in the XRD patterns of the reduced sample. We attempted to introduce preferential orientations for both the metallic Pt and the $LaFeO_3$- and $LaAlO_3$-related phases in the Rietveld refinement of the XRD patterns; however, the quality of the fit did not improve.

3.3. CO-Oxidation Rates. Differential CO-oxidation rates were measured in 25 Torr CO and 12.5 Torr O_2 on Pt/$LaFeO_3$/$MgAl_2O_4$ (2.9 wt % Pt, 30 wt % $LaFeO_3$), Pt/FeO_x/$MgAl_2O_4$ (3.0 ± 0.2 wt % Pt, 10 ± 1 wt % Fe_2O_3), and Pt/$MgAl_2O_4$ (3.1 ± 0.2 wt % Pt) samples. All of the samples were prepared by ALD, with the Pt loadings achieved by the amount of Pt added in 1 ALD cycle. To determine the effect of pretreatment conditions, we performed the initial measurements on each catalyst prior to any redox treatments. After ALD deposition of Pt, the catalysts were calcined to only 573 K to remove the ligands on the Pt precursor before measuring the "as-prepared" rates. Rate measurements were then obtained on each of the catalysts after oxidation at 1073 K, after reduction at 1073 K, and after 5 redox cycles. Arrhenius plots for Pt/$LaFeO_3$/$MgAl_2O_4$ are shown in Figure 6, whereas the analogous plots for Pt/FeO_x/$MgAl_2O_4$ and Pt/$MgAl_2O_4$ are reported in Figure S13. Light-off profiles for Pt/$LaFeO_3$/$MgAl_2O_4$ are shown in Figure S14 and are consistent with data in Figure 6. Rates on the as-prepared Pt/$LaFeO_3$/$MgAl_2O_4$ were high and it was necessary to obtain the data at relatively low temperatures to achieve differential conditions for the catalyst loading and flow rates that were used. When not promoted by a reducible oxide,[17] CO-oxidation rates on Pt are dependent only on the metal surface area.[18] Using these rates from the literature,[19] we estimated the Pt dispersion of the as-prepared catalyst to be 26%, in good agreement with room-temperature CO chemisorption measurements, as shown in Table 3. When this catalyst was calcined to 1073 K, the rates decreased a factor of about 25, but the rates returned to their initial value after reduction at 1073 K. Repeated oxidation and reduction cycles at 1073 K caused the catalyst to go between the active and inactive states.

Activation and deactivation of the Pt/$LaFeO_3$/$MgAl_2O_4$ cannot be due simply to oxidation or reduction of the Pt.

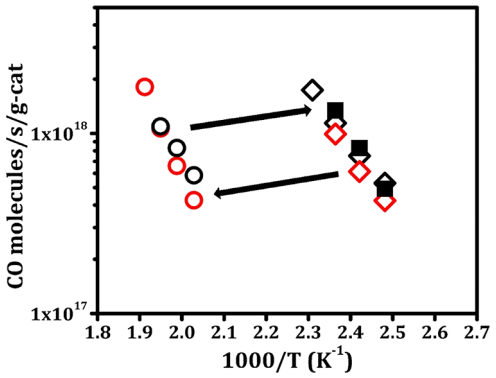

Figure 6. Steady-state, differential reaction rates for CO oxidation with 25 Torr CO and 12.5 Torr O_2 for a 0.1-g sample of Pt/$LaFeO_3$/$MgAl_2O_4$. Rates measured on the as-prepared sample are marked in solid squares. Rates measured on the sample after oxidation in 10% O_2–He at 1073 K for 1 h are marked in circles; rates measured on the sample after reduction in 10% H_2–He at 1073 K for 1 h are marked in diamonds. Black symbols denote the first redox cycle, whereas red symbols denote the fifth cycle.

First, as shown in Figure S15, reduction at 773 K did not restore activity in a catalyst that had been oxidized at 1073 K and oxidation at 773 K did not deactivate a catalyst that had been reduced at 1073 K. Furthermore, deactivation of the oxidized catalyst cannot be due to reversible formation of Pt single atoms, as has been reported in other studies,[21,22] because that would be inconsistent with the STEM and XRD data. That the reduced Pt/$LaFeO_3$/$MgAl_2O_4$ exhibited superior activity supports the fact that the Pt is likely in the dispersed form because the CO-oxidation rate is directly proportional to the surface metal dispersion. There was also a major change in the catalyst after the first high-temperature oxidation cycle in that we were not able to measure dispersion by CO chemisorption. As shown in Table 3, adsorption of CO at room temperature was negligible after high-temperature treatments, even though dispersions estimated from the reaction rates were very high. This suggests that the CO-oxidation reaction on Pt/$LaFeO_3$/$MgAl_2O_4$ is significantly different from that which occurs on normal Pt catalysts. In agreement with this, reaction orders for CO on the Pt/$LaFeO_3$/$MgAl_2O_4$, shown in Figure S16, were almost zero, whereas the reaction is normally inverse-first-order on conventional Pt.[23] Also, the activation energy for CO oxidation over reduced Pt/$LaFeO_3$/$MgAl_2O_4$, 60 ± 5 kJ/mol, was significantly lower than the activation energies calculated for Pt/$MgAl_2O_4$, 100 ± 5 kJ/mol.

The failure to observe CO chemisorption, and the weaker dependence of the reaction on CO partial pressure over Pt/$LaFeO_3$/$MgAl_2O_4$, suggests that the reaction mechanism is different. It is likely that the reaction occurs at the interface between Pt and the $LaFeO_3$ support, similar to what has been observed on Pt-CeO_2 catalysts.[24] In addition to the change in reaction order, reaction at the metal–oxide interface could also explain the decreased activation energy compared to that of the conventional Pt catalyst.

To ensure that the reaction results on Pt/$LaFeO_3$/$MgAl_2O_4$ are not due to the ALD preparation or the presence of FeO_x, we also performed reaction measurements on the Pt/$MgAl_2O_4$[20] and Pt/FeO_x/$MgAl_2O_4$ catalysts, with results shown in Figure S13. The as-prepared Pt/$MgAl_2O_4$ exhibited similar rates to those observed on as-prepared Pt/$LaFeO_3$/

Table 3. Summary of Pt Dispersion (%) Measured by CO Chemisorption or Estimated on the basis of Dispersion and Activity of Pt (111) in the Literature for Catalysts after the Fifth Reduction and Oxidation Pretreatments at 1073 K

	as-prepared		1073 K oxidized		1073 K reduced	
	measured	estimated	measured	estimated	measured	estimated
$Pt/LaFeO_3/MgAl_2O_4$	23	26	–[a]	0.2	–[a]	30
$Pt/FeO_x/MgAl_2O_4$	24	>100	0.9	0.3	1.1	0.6
$Pt/MgAl_2O_4$	27	23.5	0.1	0.1	0.1	0.4

[a]Not able to be measured.

$MgAl_2O_4$. The rates again decreased dramatically upon high-temperature calcination but were not restored by high-temperature reduction. As shown in Table 3, the dispersions estimated from the specific reaction rates agreed well with dispersions determined by CO chemisorption and the STEM measurements reported earlier (Figure S3). Rates on as-prepared $Pt/FeO_x/MgAl_2O_4$ were very high. Promotion of CO-oxidation rates on Pd catalyst due to contact with FeO_x has been reported previously[25] and is likely responsible for the high rates reported here. However, high-temperature redox cycling again resulted in a dramatic decrease in rates that could not be restored. STEM images of the $Pt/FeO_x/MgAl_2O_4$ catalyst, shown in Figure S17, demonstrated a large growth in the Pt particles and segregation of the FeO_x. Finally, a previous report of $Pt/La_2O_3/MgAl_2O_4$ also showed strong deactivation of the catalyst following redox cycling.[20]

4. DISCUSSION

Maintaining high metal dispersions in supported-metal catalysts upon high-temperature redox cycling is extremely challenging and could have important implications for catalysts operating under harsh conditions, such as those experienced by automotive emissions-control catalysts. The present work demonstrates thin $LaFeO_3$ films may be capable of achieving this important goal. This could have important commercial consequences by allowing the use of reduced amounts of precious metals in these applications.

The observation that metal particles are oriented with respect to the perovskite film indicates that there must be strong bonding interactions between the metal and perovskite. It is likely that similar bonding interactions are present with bulk perovskites and that these are at least partially responsible for the exsolution phenomenon observed in some bulk perovskites. These bonding interactions are specific to the particular metal and perovskite. For example, it has been reported that Pt can enter the perovskite lattice for both the $CaTiO_3$ and $LaFeO_3$, whereas Pd can enter only the $LaFeO_3$ lattice, not that of $CaTiO_3$.[3] Related to this, recent work also found evidence for strong support interactions with Pt, not with Pd, on thin $CaTiO_3$ films.[26] The perovskite structure must be important because we did not observe similar stabilities for Pt particles when La_2O_3 or FeO_x were deposited individually. Finally, the strength of the bonding interactions varies with the specific metal and perovskite. Although there was evidence for strong support interactions for Pt on thin $CaTiO_3$ films, relatively large Pt particles were still formed upon high-temperature redox cycling.

The properties of the Pt are clearly affected by interactions with the $LaFeO_3$ film, as demonstrated by the fact that CO adsorption is suppressed and both the reaction order and activation energy for CO oxidation are affected. Because electronic interactions can extend a few atomic distances, this may be related to the fact that a significant fraction of Pt particles are very small in the present work, so the Pt atoms at the surface of the particles must be close to the support interface. However, we cannot rule out the possibility that Pt can go beneath the surface of the perovskite, especially following oxidation. This could help explain the large difference in activity between the oxidized and reduced samples. The fact that such high temperatures are required to cycle the perovskite-containing catalysts between "activated" and "deactivated" states suggests that oxidation and reduction cause a major restructuring of the catalyst, beyond simply oxidizing and reducing the Pt surface.

There is obviously still much to learn about these perovskite-supported metals. The catalytic properties of these materials are clearly very different from that of conventional supported-metal catalysts. The fact that they can exist in a deactivated state following high-temperature oxidation also implies that they can be pretreated and used in an appropriate manner. However, the fact that one can maintain very high dispersions under very harsh conditions makes the materials very intriguing and worth additional consideration.

5. CONCLUSION

In this work, we successfully prepared a high-surface-area $LaFeO_3$ thin film on a $MgAl_2O_4$ support using ALD. We demonstrated that, following high-temperature reduction, Pt on $LaFeO_3/MgAl_2O_4$ was able to exhibit superior activity for CO oxidation, even following harsh pretreatments. $Pt/LaFeO_3/MgAl_2O_4$ was found to switch between "active" and "inactive" states for CO oxidation after high-temperature reduction or oxidation. Stabilization of Pt particle size results from strong interactions between the Pt and the support, as evidenced by the appearance of Pt particles that are epitaxially aligned with respect to the perovskite support.

■ ASSOCIATED CONTENT

Supporting Information

The Supporting Information is available free of charge at https://pubs.acs.org/doi/10.1021/jacs.0c00138.

Figure S1, STEM image and EDS mappings for the oxidized $Pt/LaFeO_3/MgAl_2O_4$; Figure S2, TPD/TGA for 2-propanol on $MgAl_2O_4$ and $Pt/LaFeO_3/MgAl_2O_4$; Figure S3, STEM images of $Pt/MgAl_2O_4$; Figure S4, high-resolution EDS mappings with line scan signals of the oxidized $Pt/LaFeO_3/MgAl_2O_4$; Figures S5 and S6, high-resolution STEM images of $Pt/LaFeO_3/MgAl_2O_4$ samples; Figure S7, XRD patterns of $Pt/LaFeO_3/MgAl_2O_4$ after the first redox cycle; Figure S8, Rietveld refinements of $Pt/LaFeO_3/MgAl_2O_4$ samples; Table S1, results from Rietveld analysis of the XRD patterns of the oxidized and reduced $Pt/MgAl_2O_4$; Figure S9, XRD and Rietveld refinements of $Pt/MgAl_2O_4$ after 5 redox

cycles; Figures S10−S12, XANES spectra, and extracted and Fourier-transformed EXAFS spectra of $Pt/LaFeO_3/MgAl_2O_4$ samples; Figure S13, Arrhenius plots of CO-oxidation rates on samples of $Pt/MgAl_2O_4$ and $Pt/FeO_x/MgAl_2O_4$; Figure S14, light-off profiles for CO oxidation on $Pt/LaFeO_3/MgAl_2O_4$; Figure S15, Arrhenius plots of CO-oxidation rates on samples of $Pt/LaFeO_3/MgAl_2O_4$ after different pretreatments; Figure S16, dependence of CO-oxidation rates on P(CO) over the reduced $Pt/LaFeO_3/MgAl_2O_4$; Figure S17, STEM and EDS mappings of the oxidized $Pt/FeO_x/MgAl_2O_4$ (PDF)

AUTHOR INFORMATION

Corresponding Author

Raymond J. Gorte − *Department of Chemical and Biomolecular Engineering and Department of Materials Science and Engineering, University of Pennsylvania, Philadelphia, Pennsylvania 19104, United States*; Email: gorte@seas.upenn.edu

Authors

Xinyu Mao − *Department of Chemical and Biomolecular Engineering, University of Pennsylvania, Philadelphia, Pennsylvania 19104, United States*; orcid.org/0000-0002-8625-2617

Alexandre C. Foucher − *Department of Materials Science and Engineering, University of Pennsylvania, Philadelphia, Pennsylvania 19104, United States*; orcid.org/0000-0001-5042-4002

Tiziano Montini − *Department of Chemical and Pharmaceutical Sciences, University of Trieste, Trieste 34127, Italy*

Eric A. Stach − *Department of Materials Science and Engineering, University of Pennsylvania, Philadelphia, Pennsylvania 19104, United States*; orcid.org/0000-0002-3366-2153

Paolo Fornasiero − *Department of Chemical and Pharmaceutical Sciences, University of Trieste, Trieste 34127, Italy*; orcid.org/0000-0003-1082-9157

Complete contact information is available at: https://pubs.acs.org/10.1021/jacs.0c00138

Notes

The authors declare no competing financial interest.

ACKNOWLEDGMENTS

This work was funded by the Department of Energy, Office of Basic Energy Sciences, Chemical Sciences, Geosciences and Biosciences Division, Grant No. DE-FG02-13ER16380. A.C.F. acknowledges the Vagelos Institute for Energy Science and Technology at the University of Pennsylvania for a graduate/postdoctoral fellowship. The authors acknowledge SOLEIL for provision of synchrotron radiation facilities and thank Dr. E. Fonda for technical assistance in using beamline SAMBA. T.M. and P.F. acknowledge the University of Trieste, MIUR (through the FFABR 2017 project), INSTM Consortium, and ICCOM-CNR for financial support.

REFERENCES

(1) Nishihata, Y.; Mizuki, J.; Akao, T.; Tanaka, H.; Uenishi, M.; Kimura, M.; Okamoto, T.; Hamada, N. Self-regeneration of a Pd-perovskite catalyst for automotive emissions control. *Nature* **2002**, *418* (6894), 164−167.

(2) Tanaka, H.; Tan, I.; Uenishi, M.; Kimura, M.; Dohmae, K. Regeneration of palladium subsequent to solid solution and segregation in a perovskite catalyst: an intelligent catalyst. *Top. Catal.* **2001**, *16*−*17* (1−4), 63−70.

(3) Tanaka, H.; Taniguchi, M.; Uenishi, M.; Kajita, N.; Tan, I.; Nishihata, Y.; Mizuki, J.; Narita, K.; Kimura, M.; Kaneko, K. Self-regenerating Rh- and Pt-based perovskite catalysts for automotive-emissions control. *Angew. Chem., Int. Ed.* **2006**, *45* (36), 5998−6002.

(4) Katz, M. B.; Zhang, S.; Duan, Y.; Wang, H.; Fang, M.; Zhang, K.; Li, B.; Graham, G. W.; Pan, X. Reversible precipitation/dissolution of precious-metal clusters in perovskite-based catalyst materials: Bulk versus surface re-dispersion. *J. Catal.* **2012**, *293*, 145−148.

(5) Kim, K. J.; Han, H.; Defferriere, T.; Yoon, D.; Na, S.; Kim, S. J.; Dayaghi, A. M.; Son, J.; Oh, T.-S.; Jang, H. M.; Choi, G. M. Facet-Dependent in situ Growth of Nanoparticles in Epitaxial Thin Films: The Role of Interfacial Energy. *J. Am. Chem. Soc.* **2019**, *141* (18), 7509−7517.

(6) Dai, S.; Zhang, S. Y.; Katz, M. B.; Graham, G. W.; Pan, X. Q. In Situ Observation of Rh-$CaTiO_3$ Catalysts during Reduction and Oxidation Treatments by Transmission Electron Microscopy. *ACS Catal.* **2017**, *7* (3), 1579−1582.

(7) Katz, M. B.; Graham, G. W.; Duan, Y. W.; Liu, H.; Adamo, C.; Schlom, D. G.; Pan, X. Q. Self-Regeneration of Pd-$LaFeO_3$ Catalysts: New Insight from Atomic-Resolution Electron Microscopy. *J. Am. Chem. Soc.* **2011**, *133* (45), 18090−18093.

(8) Onn, T. M.; Monai, M.; Dai, S.; Fonda, E.; Montini, T.; Pan, X. Q.; Graham, G. W.; Fornasiero, P.; Gorte, R. J. Smart Pd Catalyst with Improved Thermal Stability Supported on High-Surface-Area $LaFeO_3$ Prepared by Atomic Layer Deposition. *J. Am. Chem. Soc.* **2018**, *140* (14), 4841−4848.

(9) Dasgupta, N. P.; Liu, C.; Andrews, S.; Prinz, F. B.; Yang, P. Atomic layer deposition of platinum catalysts on nanowire surfaces for photoelectrochemical water reduction. *J. Am. Chem. Soc.* **2013**, *135* (35), 12932−12935.

(10) Briois, V.; Fonda, E.; Belin, S.; Barthe, L.; La Fontaine, C.; Langlois, F.; Ribbens, M.; Villain, F. SAMBA: The 4−40 keV X-ray absorption spectroscopy beamline at SOLEIL. In *Proceedings of UVX 2010-10e Colloque sur les Sources Cohérentes et Incohérentes UV, VUV et X; Applications et Développements Récents*; EDP Sciences: 2010; pp 41−47.

(11) Ravel, B.; Newville, M. ATHENA, ARTEMIS, HEPHAESTUS: data analysis for X-ray absorption spectroscopy using IFEFFIT. *J. Synchrotron Radiat.* **2005**, *12* (4), 537−541.

(12) Yeh, Y.-H.; Zhu, S.; Staiber, P.; Lobo, R. F.; Gorte, R. J. Zn-promoted H-ZSM-5 for endothermic reforming of n-hexane at high pressures. *Ind. Eng. Chem. Res.* **2016**, *55* (14), 3930−3938.

(13) Li, W.-Z.; Kovarik, L.; Mei, D.; Liu, J.; Wang, Y.; Peden, C. H. Stable platinum nanoparticles on specific $MgAl_2O_4$ spinel facets at high temperatures in oxidizing atmospheres. *Nat. Commun.* **2013**, *4* (1), 2481.

(14) Holder, C. F.; Schaak, R. E. Tutorial on Powder X-ray Diffraction for Characterizing Nanoscale Materials. *ACS Nano* **2019**, *13* (7), 7359−7365.

(15) Shannon, R. T.; Prewitt, C. T. Effective ionic radii in oxides and fluorides. *Acta Crystallogr., Sect. B: Struct. Crystallogr. Cryst. Chem.* **1969**, *25* (5), 925−946.

(16) Vaarkamp, M. Obtaining reliable structural parameters from EXAFS. *Catal. Today* **1998**, *39* (4), 271−279.

(17) Bera, P.; Gayen, A.; Hegde, M. S.; Lalla, N. P.; Spadaro, L.; Frusteri, F.; Arena, F. Promoting effect of CeO_2 in combustion synthesized Pt/CeO_2 catalyst for CO oxidation. *J. Phys. Chem. B* **2003**, *107* (25), 6122−6130.

(18) Haneda, M.; Watanabe, T.; Kamiuchi, N.; Ozawa, M. Effect of platinum dispersion on the catalytic activity of Pt/Al_2O_3 for the oxidation of carbon monoxide and propene. *Appl. Catal., B* **2013**, *142*, 8−14.

(19) Rodriguez, J. A.; Goodman, D. W. High-Pressure Catalytic Reactions over Single-Crystal Metal-Surfaces. *Surf. Sci. Rep.* **1991**, *14* (1−2), 1−107.
(20) Mao, X.; Foucher, A. C.; Stach, E. A.; Gorte, R. J. Intelligent" Pt Catalysts Based on Thin $LaCoO_3$ Films Prepared by Atomic Layer Deposition. *Inorganics* **2019**, *7* (9), 113.
(21) Jones, J.; Xiong, H.; DeLaRiva, A. T.; Peterson, E. J.; Pham, H.; Challa, S. R.; Qi, G.; Oh, S.; Wiebenga, M. H.; Pereira Hernandez, X. I.; Wang, Y.; Datye, A. K. Thermally stable single-atom platinum-on-ceria catalysts via atom trapping. *Science* **2016**, *353* (6295), 150−154.
(22) Gänzler, A. M.; Casapu, M.; Vernoux, P.; Loridant, S.; Cadete Santos Aires, F. J.; Epicier, T.; Betz, B.; Hoyer, R.; Grunwaldt, J. D. Tuning the structure of platinum particles on ceria in situ for enhancing the catalytic performance of exhaust gas catalysts. *Angew. Chem., Int. Ed.* **2017**, *56* (42), 13078−13082.
(23) Kale, M. J.; Christopher, P. Utilizing quantitative in situ FTIR spectroscopy to identify well-coordinated Pt atoms as the active site for CO oxidation on Al_2O_3-supported Pt catalysts. *ACS Catal.* **2016**, *6* (8), 5599−5609.
(24) Cargnello, M.; Doan-Nguyen, V. V.; Gordon, T. R.; Diaz, R. E.; Stach, E. A.; Gorte, R. J.; Fornasiero, P.; Murray, C. B. Control of metal nanocrystal size reveals metal-support interface role for ceria catalysts. *Science* **2013**, *341* (6147), 771−773.
(25) Mao, X.; Foucher, A.; Stach, E. A.; Gorte, R. J. A Study of Support Effects for CH_4 and CO Oxidation over Pd Catalysts on ALD-Modified Al_2O_3. *Catal. Lett.* **2019**, *149* (4), 905−915.
(26) Lin, C.; Foucher, A. C.; Ji, Y.; Curran, C. D.; Stach, E. A.; McIntosh, S.; Gorte, R. J. Intelligent" Pt Catalysts Studied on High-Surface-Area $CaTiO_3$ Films. *ACS Catal.* **2019**, *9* (8), 7318−7327.